

# Multiferroic phases of the frustrated quantum spin-chain compound linarite

K. Yu. Povarov,<sup>1,\*</sup> Y. Feng,<sup>1</sup> and A. Zheludev<sup>1</sup>

<sup>1</sup>*Neutron Scattering and Magnetism, Laboratory for Solid State Physics, ETH Zürich, Switzerland*<sup>†</sup>

The dielectric properties of the prototypical frustrated ferromagnetic spin-chain compound  $\text{PbCuSO}_4(\text{OH})_2$  known as linarite, are studied across its strongly anisotropic magnetic phase diagram in single crystal samples. The ferroelectric character of the principal low-field spin spiral phase is confirmed. The measured polarization is fully consistent with the previously proposed magnetic structure. Spontaneous polarization is also detected in two other field-induced phases but in some cases is incompatible with previously suggested models for the spin arrangement.

## I. INTRODUCTION

The improper ferroelectric nature of magnetically ordered phases in certain antiferromagnetic materials endows them with a rich phenomenology and potential technological applications. In recent years it has given rise to the entirely new research area of *magnetic multiferroics* [1–3]. Correlations between magnetic ordering and dielectric properties have been found in very different classes of materials. On one end of the spectrum are rare earth compounds, with a large spin value and truly dramatic magnetoelectric effects [4, 5]. The other limit is  $S = 1/2$  organometallic cuprates, whose extreme quantum fluctuations fully suppress long-range order, which is only restored by a field-induced quantum phase transition [6, 7]. A more conventional type of multiferroic cuprates is systems featuring edge-sharing copper-oxygen chains. Among these are  $\text{LiCu}_2\text{O}_2$  [8] and  $\text{LiCuVO}_4$  [9], which have long served as prototype materials for the study of multiferroicity [10, 11]. In these systems the source of electric polarization is a helimagnetic arrangement of spins that breaks inversion symmetry [12, 13]. Helimagnetism, in turn, results from a geometric frustration of magnetic interactions. Specifically, the Heisenberg exchange constant  $J_1$  between the nearest-neighbor  $\text{Cu}^{2+}$  spins is ferromagnetic, and competes with the antiferromagnetic next-nearest-neighbor coupling  $J_2$ .

The most recently studied member of the frustrated copper-oxide-chain family is the natural mineral linarite  $\text{PbCuSO}_4(\text{OH})_2$  [14]. It is also perhaps the most interesting one: the estimated ratio of exchange constants  $J_1/J_2 \simeq -2.8$  places linarite very close to the quantum critical point at  $J_1/J_2 \simeq -4$ , where the ferromagnetic interaction takes over and the ground state changes to a fully polarized one. At the same time, the saturation field in linarite is below 10 T, making its entire magnetic phase diagram easily accessible experimentally [15]. To date, up to five distinct magnetic phases have been identified. This complex behavior emphasizes the highly frustrated nature of this spin system and the importance of quantum spin fluctuation [15, 16]. The primary Phase I, occurring at zero applied magnetic field, has been identified

as a spin spiral. It would be natural to expect this phase to generate nonzero electric polarization, simply by analogy to  $\text{LiCu}_2\text{O}_2$  and  $\text{LiCuVO}_4$ . Indeed, previous studies have detected the presence of bias-induced electric polarization in linarite *powder* samples below  $T_N$  [17]. The challenge, remains to perform more detailed studies on a *single-crystal* sample, in order to determine the direction of polarization, its relation to the underlying magnetic order, and its evolution in external magnetic fields. This is the issue addressed in the present study.

Blue transparent crystals of linarite belong to the monoclinic  $P2_1/m$  (No. 11) space group. The unit cell dimensions are  $a = 9.68$ ,  $b = 5.65$ ,  $c = 4.68$  Å, with the angle between  $a$  and  $c$  being  $\beta = 102.6^\circ$  [18]. The structure of the material is shown in Fig. 1. There are two copper atoms per unit cell. Together with surrounding oxygen ions they form a ribbon chain of Cu-O plaquettes, propagating along the high-symmetry  $\mathbf{b}$  direction. Magnetization measurements supported by first-principle calculations lead to estimates of the main exchange parameters of  $J_1 \simeq -8.6$  and  $J_2 \simeq 3.1$  meV [19]. A rich magnetic phase diagram (Fig. 2) was revealed below  $T_N \simeq 2.8$  K [15, 16]. Five distinct magnetic phases exist for  $\mathbf{H} \parallel \mathbf{b}$ . The zero-field elliptic spin spiral (I) changes to a canted commensurate structure (IV) around 3 T, with the transition line splitting into regions of phase coexistence at low and high temperatures. The high-temperature region, labeled III, is supposed to be a mixture of Phase IV and alternative spiral configuration, different from Phase I. The low-temperature II region is a metastable mixture of Phases I and IV. Finally, for  $\mathbf{H} \parallel \mathbf{b}$ , there is an unusual high-field phase believed to be a spin-density wave state (V). Remarkably, for a magnetic field applied transverse to the  $\mathbf{b}$  direction, there appears to be only a single magnetic phase, namely, the spiral state I.

## II. EXPERIMENTAL DETAILS

The present study employed natural single crystals of linarite from the Grand Reef Mine, Arizona, USA. For all samples, the crystal structure was verified at room temperature by means of x-ray diffraction (BRUKER APEX II single-crystal diffractometer), and found to be in good agreement with the previously published data [15, 20].

\* povarovk@phys.ethz.ch

<sup>†</sup> <http://www.neutron.ethz.ch/>

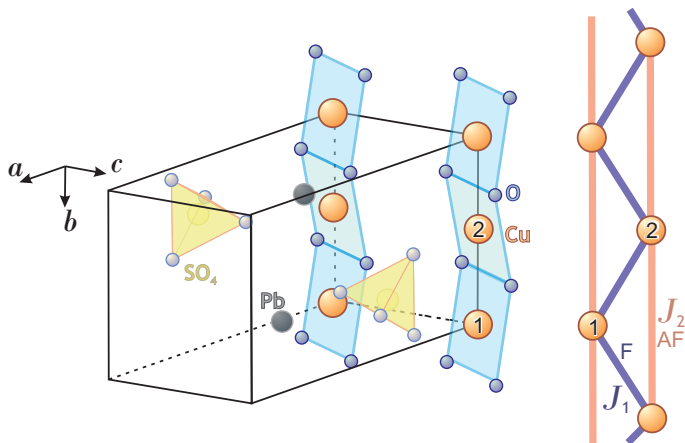


FIG. 1. Left: Crystal structure of linarite  $\text{PbCuSO}_4(\text{OH})_2$ . The two copper positions are labeled. Hydrogen atoms adjacent to the in-chain oxygen atoms are omitted for clarity. Right: The corresponding diagram of a basic in-chain Heisenberg Hamiltonian with ferromagnetic  $J_1$  and antiferromagnetic  $J_2$  interactions (values are given in the text).

We have also carefully checked the magnetic phase diagram of our samples and found it to be consistent with previous studies. As will be reported in detail elsewhere, to that end we used standard SQUID magnetometry (Quantum Design MPMS) and a home-built cantilever torque magnetometry setup. The corresponding experimental points, obtained for several samples, are shown in Fig. 2 (rhombi and crosses), in direct comparison with phase boundaries reported in Ref. [16] (lines).

For our dielectric experiments we have carefully selected a number of single crystals in which either the [100] or the [001] faces were well developed, and where the  $\mathbf{b}$  direction could be clearly identified. The initial choice was based on the morphology [21], which was further verified by x-ray diffraction. The typical area of such faces was  $1 - 2 \text{ mm}^2$ , with a typical transverse sample thickness of about  $0.5 \text{ mm}$ . The crystalline plates thus selected were sandwiched between external field electrodes (see Fig. 3). Correspondingly, the dielectric properties were probed along either the  $\mathbf{a}^*$  [22] or  $\mathbf{c}^*$  directions. For each of these two cases, we used three principal measurement geometries:  $\mathbf{H} \parallel \mathbf{b}$ ,  $\mathbf{H} \parallel \mathbf{e}$  and  $\mathbf{H} \parallel \mathbf{b} \times \mathbf{e}$ , where  $\mathbf{e}$  is the direction transverse to the electrodes. The dielectric permittivity was measured by an Andeen–Hagerling 2550A capacitance bridge using a 3-terminal scheme. Pyroelectric current measurements were performed with a Keithley 617A electrometer.

All experiments were carried out in the standard Dilution Refrigerator inset in the Quantum Design 9 T PPMS. This imposed some limitations on the types of pyro- or magnetoelectric current scans that could be performed: measuring current vs.  $T$  was feasible only in the range  $1 - 4 \text{ K}$  in the evaporative mode of Dilution Refrigerator operation. This configuration allowed us to achieve a good signal-to-noise ratio at a temperature sweep rate

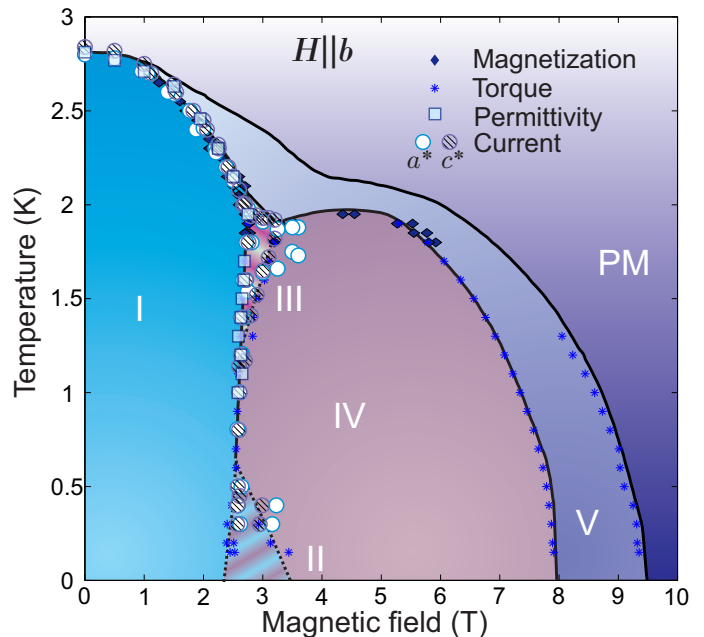


FIG. 2. Phase diagram of linarite for a field applied along the  $\mathbf{b}$  direction. Following Ref. [16] the distinct thermodynamic phases are an elliptical spiral (I), a collinear Néel antiferromagnetic phase (IV), a spin-density wave (V), and a circular helix coexisting with collinear ordering (III). Phase II is supposed to be a metastable mixture of Phases I and IV. Solid lines are the phase boundaries according to Ref. [16]; symbols are the results of this work.

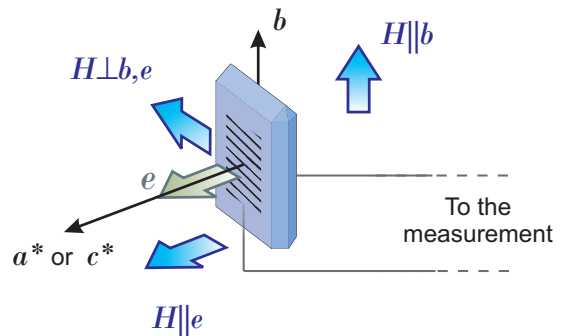


FIG. 3. Measurement schematics. A small crystal of linarite has electrodes connected to its principal surface, either [100] or [001], while the  $\mathbf{b}$  axis is in the elongated direction. This corresponds to measuring the dielectric properties (in the direction given by  $\mathbf{e}$ ) along either  $\mathbf{a}^*$  or  $\mathbf{c}^*$ . Three naturally possible orientations of the external magnetic field are also shown.

of  $0.5 \text{ K/min}$ , while the difference between heating and cooling data sets remained negligible. In the dilution cooling regime below  $1 \text{ K}$  the increase in thermal coupling times prevented a collection of meaningful current data in temperature sweeps. In contrast, measurements of current vs.  $H$  were possible at all temperatures down to approximately  $0.2 \text{ K}$  at an optimal sweeping rate of

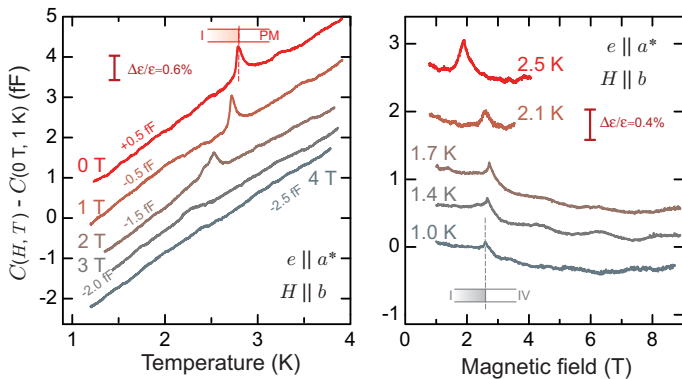


FIG. 4. Examples of measured  $\mathbf{a}^*$ -dielectric permittivity anomalies in linarite in a magnetic field along the  $\mathbf{b}$  direction. Data are plotted as the difference between the measured capacitance and the reference value observed at  $T = 1$  K,  $H = 0$  T. In the left panel some constant offsets are additionally introduced for clarity. Phase boundaries according to Ref. [16] are shown for some of the curves.

0.01 T/s.

### III. RESULTS

#### A. Magnetic field along the $\mathbf{b}$ axis

Figure 4 shows a number of representative dielectric permittivity scans, measured with the electric field along the  $\mathbf{a}^*$  direction. In contrast to the previous study by Yasui *et al.* [17], we do indeed find well-defined peaks in the dielectric permittivity occurring at the boundaries of Phase I. They are, unfortunately, too weak for a more quantitative investigation, but serve as markers of the phase transition and reveal the electrically active nature of Phase I. In the phase diagram in Fig. 2, their positions are plotted as squares. No further permittivity anomalies were detected in magnetic fields exceeding 3 T. Unfortunately, due to the small size of the sample the measurement background is non-negligible and this prevents us from precisely calibrating the vertical scale in Fig. 4 in the sample's dielectric permittivity units. However, from the data we can estimate  $\varepsilon \simeq 20$  in the vicinity of  $T_N$ . This is in agreement with the earlier measurements by Yasui *et al.* [17]. The magnitude of the zero-field anomaly is then estimated as only  $\Delta\varepsilon/\varepsilon \simeq 6 \cdot 10^{-3}$ , and it weakens progressively in the applied magnetic field.

The phenomenology of current anomalies turned out to be much richer and easier to investigate. An important point is that we found the charge flow associated with the magnetic ordering to occur *spontaneously*, without any external voltage applied to the sample. Furthermore, moderate bias voltages (from +250 to -250 V) applied to the sample during the cooldown process were able to change the amount of the accumulated charge by only  $\pm 30\%$  without causing a polarization sign reversal. This

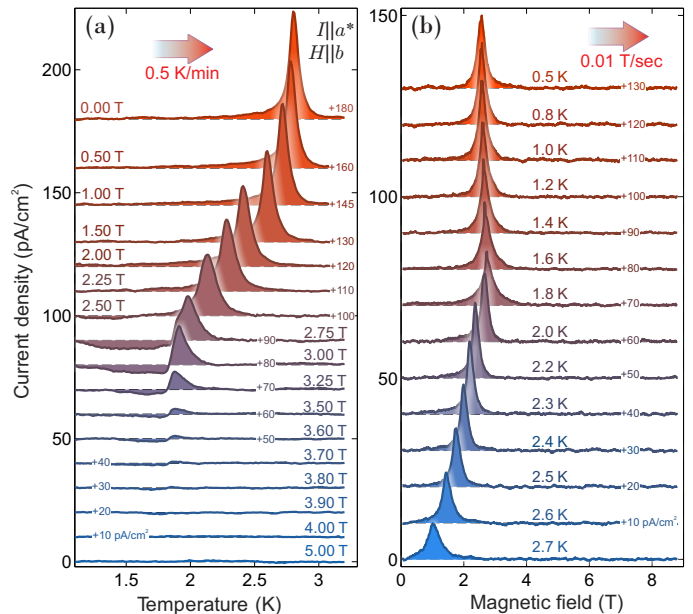


FIG. 5. Spontaneous current  $I_{a^*}$  through the sample (no bias voltage applied) in a magnetic field applied along the  $\mathbf{b}$  direction. (a) The pyroelectric current as a function of the temperature during the warm-up; (b) the magnetoelectric current in an increasing magnetic field. Offsets are explicitly indicated. The zero level for each curve is shown by a dashed line.

clearly indicates the existence of a preferred polarization direction, which is somewhat surprising for a centrosymmetric space group (such as  $P2_1/m$  of linarite). Possible explanations of this finding are discussed in Sec. IV B.

The pyroelectric current  $I_{a^*}$  measured in temperature sweeps at several values of applied field is plotted in Fig. 5(a). In zero magnetic field there is a prominent peak with a maximum at  $T_N \simeq 2.8$  K. This peak gradually broadens and shifts to lower temperatures with increasing field up to approximately 2.5 T. At this point, upon cooling, one enters the region labeled III in Fig. 2. Here the pyroelectric current develops a more complex two-peak structure. First, charge goes into the sample during the cooldown into Phase III, and then it exits upon further cooling towards the Phase IV. Above 3.6 T no transition-related features in the pyroelectric current could be resolved at these temperatures. This shows the apparent nonelectric character of Phases IV and V.

Isothermal magnetolectric current measurements provide a complementary way of accessing the polarization. The field dependence of  $I_{a^*}$  is plotted in Fig. 5(b) for several temperatures. At first glance there is just a single peak corresponding to the charge released upon exiting Phase I. However, additionally there is a sharp current spike on top of the broader peak between 0.5 and 1.5 K. This marks a polarization discontinuity along what is a first-order phase transition line. The discontinuity becomes somewhat softened at the lowest temperatures, when another region of phase coexistence is

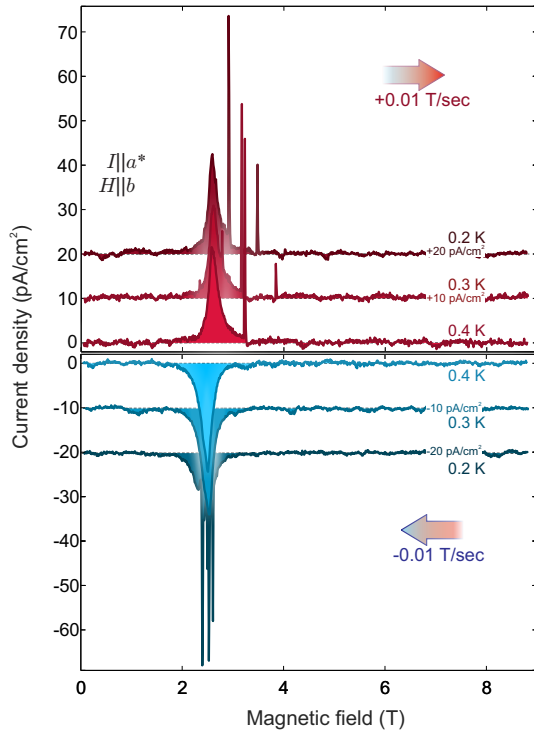


FIG. 6. Examples of up and down field scans of the  $I_{a^*}$  current below  $T = 0.5$  K. The magnetic field is applied along the  $\mathbf{b}$  direction. The difference in the scans with increasing vs decreasing  $H$ , as well as the complex multi-peak response, is related to the metastability of Phase II.

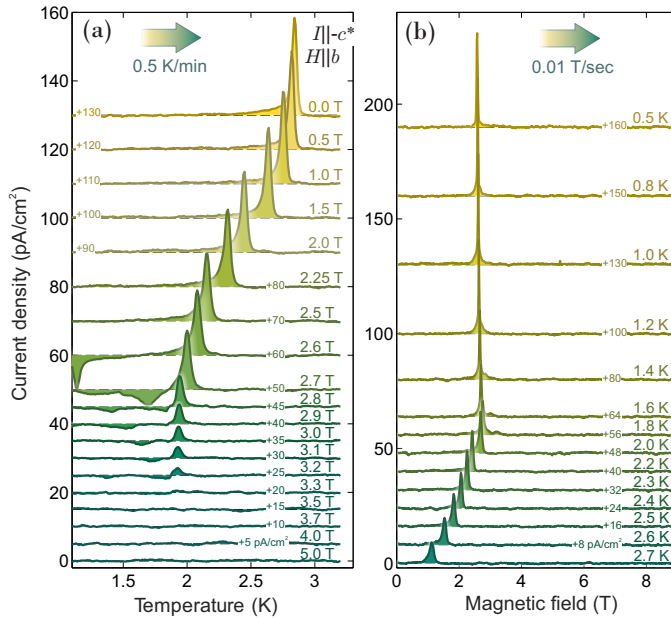


FIG. 7. The same as Fig. 5, but for the  $I_{c^*}$  component of the current.

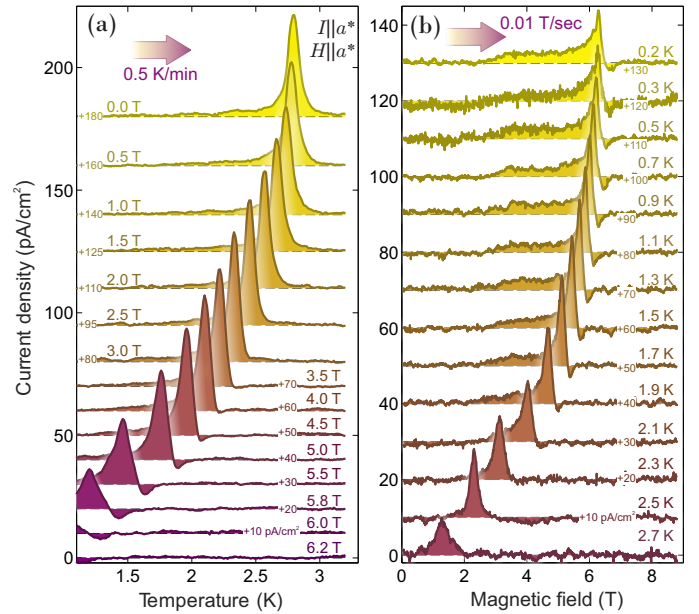


FIG. 8. The same as Fig. 5, but for the magnetic field  $\mathbf{H} \parallel \mathbf{a}^*$ .

approached (Phase II in the Fig. 2 phase diagram). As shown in Fig. 6, a rather complex behavior emerges below 0.5 K. Upon lowering the temperature the main peak becomes accompanied by multiple history-dependent sharp satellites. This directly reflects the metastable nature of Phase II [15]. No additional features could be found at higher magnetic fields at any temperature.

For the  $\mathbf{c}^*$  component of the current the situation is qualitatively similar. Examples of the  $I_{c^*}$  scans are shown in Fig. 7. The main difference is the weaker and much more abrupt character of the corresponding anomalies. The peaks in  $I_{c^*}$  are much narrower than in  $I_{a^*}$  at similar temperatures. This is especially pronounced below 1 K at the first-order transition from Phase I to Phase IV. At temperatures below 0.5 K a hysteretic multipole structure develops, similarly to that in  $I_{a^*}$  described above.

## B. Magnetic field along the $\mathbf{a}^*$ and $\mathbf{a}$ directions

Anomalies occurring in the current  $I_{a^*}$  as a function of temperature and magnetic field along the  $\mathbf{a}^*$  direction are shown in Fig. 8. In small fields, the pyroelectric current behaves in a way similar to the  $\mathbf{H} \parallel \mathbf{b}$  case. However, at higher fields a surprising two-peak structure is observed. The reversal of current direction corresponds to polarization reversal upon cooling. This behavior is also well pronounced in field scans [Fig. 8(b)] at lower temperatures. The charge release is slower than in the  $\mathbf{H} \parallel \mathbf{b}$  case. This is why the amplitude of the  $I_{a^*}$  anomaly is seemingly reduced. Instead, the transition-related peak has a long tail stretching to low fields, reflecting the gradual evolution of the spiral structure towards the full saturation.

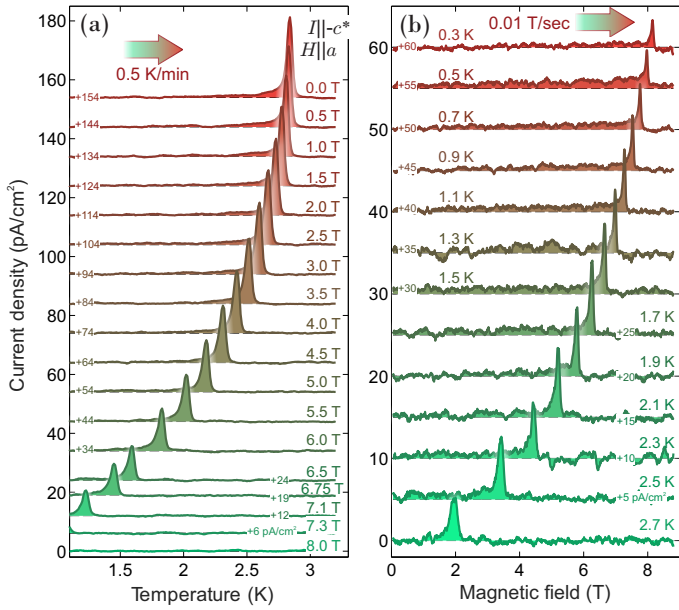


FIG. 9. The same as Fig. 7, but for the magnetic field  $\mathbf{H} \parallel \mathbf{a}$ .

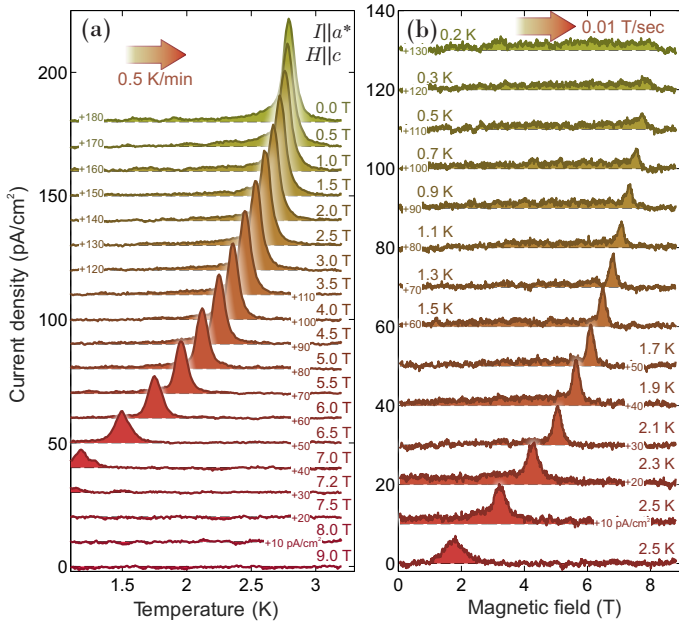


FIG. 10. The same as Fig. 5, but for the magnetic field  $\mathbf{H} \parallel \mathbf{c}$ .

The current  $I_{c^*}$  in a magnetic field applied along  $\mathbf{a}$  shows slightly different behavior (Fig. 9). We find only a single sharp peak at all fields and temperatures. In the low- $T$  regime, it develops an extended tail, similarly to the  $I_{a^*}$  case discussed above.

### C. Magnetic field along the $\mathbf{c}$ and $\mathbf{c}^*$ directions

The cases of a magnetic field applied along the  $\mathbf{c}$  and  $\mathbf{c}^*$  directions appear to be the most trivial ones. There

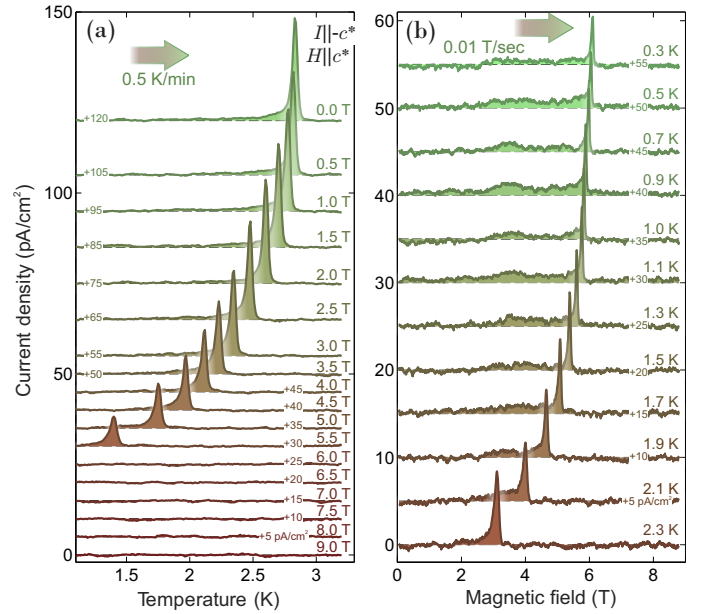


FIG. 11. The same as Fig. 7, but for the magnetic field  $\mathbf{H} \parallel \mathbf{c}^*$ .

is always a single feature in the spontaneous current occurring at the phase boundary. A summary of  $I_{a^*}$  scans is present in Fig. 10. Upon lowering the temperature the peak becomes progressively less pronounced. Below 0.5 K, instead of a peak, a small and almost-constant current is detected within the ordered phase. This corresponds to an almost-constant rate of charge release.

The  $c^*$  component of electrical current measured in a magnetic field applied along the  $\mathbf{c}^*$  direction is plotted in Fig. 11. The observed behavior is almost identical to that for  $\mathbf{H} \parallel \mathbf{a}^*$ .

## IV. DISCUSSION

### A. Polarization: A brief summary

In Fig. 12 we compare representative field and temperature dependencies of different electric polarization components. These plots are deduced from  $T$  and  $H$  dependencies of  $I_{a^*}$  and  $I_{c^*}$ , respectively, keeping in mind that the spontaneous polarization is totally absent at high fields and high temperatures. In this case the polarization change obtained by integrating the field or temperature current dependence (always along the trajectory starting in the paramagnetic phase where  $\mathbf{P} = 0$ ) is equivalent to the total polarization.

Along with the curves one can also see the associated uncertainty, estimated from the noise level during the measurement (those shaded areas also happen to be a fair estimate of the measurement reproducibility). The following phenomenology is evident from these data: in small magnetic fields the polarization emerges at the ordering temperature of Phase I, and then quickly satu-

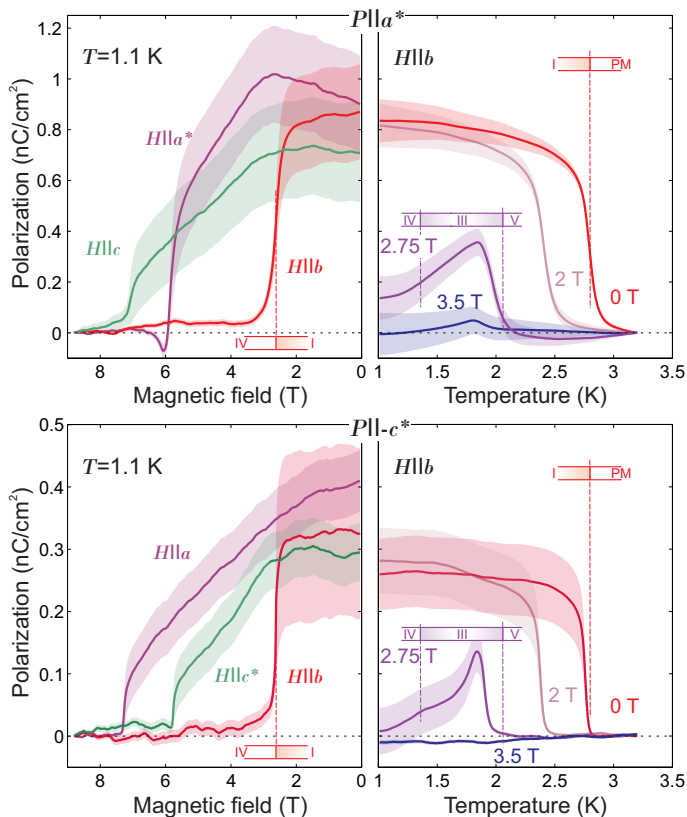


FIG. 12. Measured evolution of the polarization vector components as functions of the magnetic field and temperature. Shaded areas show respective errors accumulating during the current integration procedure. Phase boundaries according to [16] are indicated for selected polarization curves.

rates. One may argue that both components of  $\mathbf{P}(T)$  are already saturated around 1 K. For a field applied along the  $\mathbf{b}$  axis, the situation drastically changes around 2.5 T, where upon cooling one consecutively enters first Phase III, and then Phase IV. Again, both components of  $\mathbf{P}(T)$  rise around the corresponding transition temperature, but this is followed by a decrease upon further cooling. The magnitude of the polarization components is also noticeably reduced compared to those in Phase I. Finally, in higher fields, where only Phases IV and V are present, the electric polarization is absent.

The left panels in Fig. 12 show the magnetic-field dependencies for the components of  $\mathbf{P}(H)$  at  $T = 1.1$  K. For  $\mathbf{H} \parallel \mathbf{b}$  the polarization disappears in an abrupt way as the first-order phase transition from Phase I to Phase IV takes place. In contrast, for fields  $\mathbf{H} \perp \mathbf{b}$  the decrease in  $\mathbf{P}(H)$  is gradual, but with a clear onset point at the saturation field. We also would like to note the interesting behavior found in the  $P_{a^*}$  component of polarization in the magnetic field applied along  $\mathbf{a}^*$  case. Here the  $P_{a^*}$  component changes its sign before fully disappearing in the paramagnetic phase. This feature is discussed in more detail in Sec. IV E. An alternative representation of the  $P(H, T)$  data may be found in Appendix A.

The actual values of saturation fields for different field directions deserve an additional comment. Confusingly, the saturation fields are similar for  $\mathbf{H} \parallel \mathbf{a}^*, \mathbf{c}^*$  and  $\mathbf{H} \parallel \mathbf{a}, \mathbf{c}$ , but not for  $\mathbf{H} \parallel \mathbf{a}^*, \mathbf{a}$  or  $\mathbf{H} \parallel \mathbf{c}^*, \mathbf{c}$ . This appears strange, given that the mismatch between the direct and the reciprocal space vectors is only about  $13^\circ$ . The answer to the riddle is in the  $g$  tensor, completely mapped in Ref. [23]. Indeed, the principal axis of this tensor lies between the  $\mathbf{a}$  and the  $\mathbf{c}$  directions in such a way that  $g_c \simeq g_a$  and  $g_{c^*} \simeq g_{a^*}$ .

Finally, we would like to stress the difference between the  $\mathbf{P}(H)$  dependence observed here and the conventional magnetoelectric effect [24–26]. In a conventional magnetoelectric effect materials the polarization change is observed in the magnetic field due to a special symmetry-allowed bilinear term in the free energy:  $\lambda_{\alpha\beta} H_\alpha E_\beta$ . In this situation non-zero  $\mathbf{H}$  results in nonzero intrinsic  $\mathbf{E}$ , and  $\mathbf{P} \propto \mathbf{E}$ . In this case the sign of  $H$  clearly matters. In linarite the polarization is *not* magnetic field induced (It appears even in zero field!). Therefore, there is no difference between  $+H$  and  $-H$  directions of the magnetic field. Any coupling of magnetic field to polarization in our case is related to the spin spiral structure (which is insensitive to the sign of the magnetic field) as discussed in detail below.

## B. Polarization in Phase I

The magnetic structure of linarite Phase I, found by Willenberg *et al.* [18], is an elliptic spiral with the rotation plane significantly tilted with respect to the crystallographic directions. It can be formally described with the help of  $\mathbf{u}$  — a unit vector, tilted by approximately  $27^\circ$  off the  $\mathbf{a}$  axis in the  $ac$  plane. The  $ub$  plane is then the plane of the spiral rotation, as shown in Fig. 13. An additional unit vector  $\mathbf{n}$ , present in this figure, is the normal vector to this rotation plane.

As follows from Fig. 12, the polarization components in Phase I at zero external field are  $P_{a^*} = 0.8 \pm 0.1$  and  $P_{c^*} = 0.25 \pm 0.1$  nC/cm<sup>2</sup> in the low-temperature limit. This is in a rough agreement with the direction of vector  $\mathbf{u}$  (see Fig. 13). This observation is in line with the “inverse Dzyaloshinskii–Moryia” or “spin-current” mechanism [12, 13], which is a typical scenario of ferroelectric polarization appearing as a result of a spiral magnetic order. The spiral arrangement of magnetic moments breaks the inversion symmetry *within* the spiral plane, but only if the incommensurate propagation vector belongs to this plane as well. Mathematically it can be expressed as  $\mathbf{P} \propto [\mathbf{Q} \times \mathbf{n}]$ , which, in the present case, is exactly along the  $\mathbf{u}$  direction. The exact sign of  $\mathbf{P}$  is related to the spiral’s sense of rotation, or chirality (which determines the consistent choice of signs for  $\mathbf{Q}$  and  $\mathbf{n}$  vectors, with the latter defined via the cross product of adjacent spins in the chain). A typical situation is that in the ordered phase the spiral domains are forming, which differ only by the sense of spiral rota-

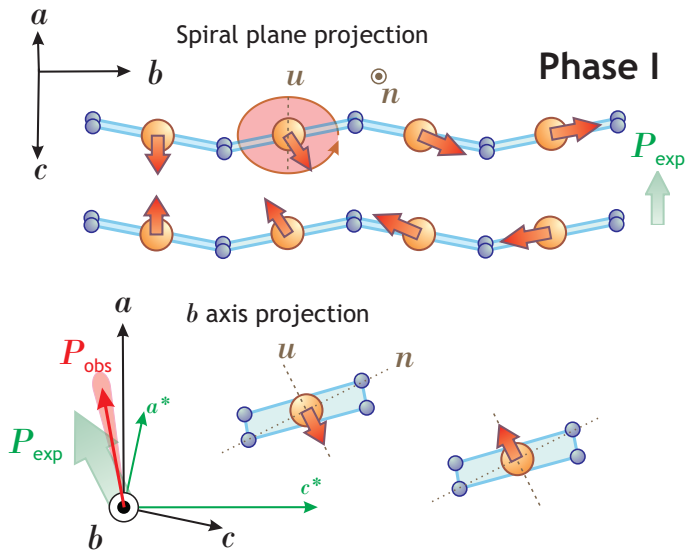


FIG. 13. The magnetic structure of Phase I according to Refs. [16, 18]. The direction of polarization dictated by the “inverse Dzyaloshinskii–Moriya mechanism” is indicated by the large green arrow. The observed polarization is shown by the red arrow, with the shaded area providing the experimental fan of uncertainty.

tion, clockwise or counterclockwise. In centrosymmetric material one would expect an approximately equal population of both types of domains, which would have the opposite directions of polarization as a consequence of the inverse Dzyaloshinskii–Moriya mechanism. An external electric field would couple to polarization and alter the domain population. This kind of behavior was clearly demonstrated for  $\text{LiCuVO}_4$ , for example [9]. In contrast, in the present measurements on centrosymmetric  $\text{PbCuSO}_4(\text{OH})_2$  the polarization direction, and thus the spin chirality, has a preferred direction even in the absence of biasing field. Furthermore, field-cooling in an applied electric field is unable to reverse the polarization. A potential explanation might be a strain in the sample, caused by the experimental environment at low temperatures. Improper ferroelectrics are known to be rather sensitive to elastic perturbations [27]. A somewhat more exciting but speculative explanation would be an unnoticed structural transition occurring at intermediate temperatures and leading to the loss of inversion symmetry. One example of a symmetry lowering transition, hardly noticeable structurally or thermodynamically, but having a profound effect on the magnetism, was recently discussed in Ref. [28].

Rigorously speaking, this unexpected symmetry breaking in linarite remains enigmatic and further work is needed to clarify this issue.

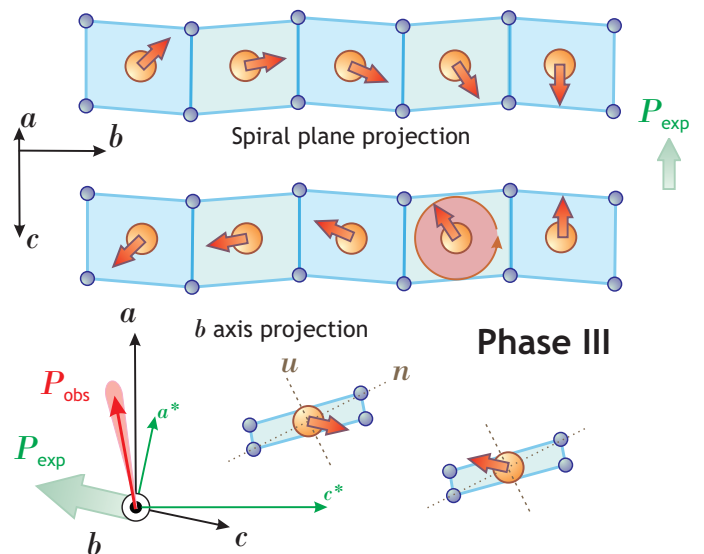


FIG. 14. Same as Fig. 13, but for the field-induced Phase III. The observed direction of polarization is inconsistent with that deduced from the proposed magnetic structure.

### C. Polarization in Phase III

Our measurements show that Phase I is not the only multiferroic phase of linarite. We also find clear signatures of ferroelectricity (mainly visible in temperature scans) in Phase III. Neutron diffraction studies in Ref. [16] have suggested this phase to be of a mixed nature, with the intensity from incommensurate magnetic Bragg peaks gradually shifting to commensurate magnetic Bragg peaks (belonging to Phase IV). At the same time, even though the incommensurate propagation vector in Phase III is the same as that in Phase I,  $\mathbf{Q} = (0, -0.186, 0.5)$  r.l.u., the spin arrangement is claimed to be different. It was identified as a circular helix with the rotation plane matching the  $(\mathbf{b}, \mathbf{c})$  plane of the crystal. As the structure is still a spin spiral, the presence of electric polarization is not surprising. However, the observed direction of  $\mathbf{P}$  is *inconsistent* with the proposed spin arrangement, as illustrated in Fig. 14. Indeed, in the inverse Dzyaloshinskii–Moriya mechanism necessarily  $\mathbf{P} \propto [\mathbf{Q} \times \mathbf{n}]$ . Therefore, a  $(\mathbf{b}, \mathbf{c})$  planar spiral strictly requires the polarization to lie *within* the spiral plane. In contrast, experimentally the largest polarization component is observed along direction  $\mathbf{a}^*$ , which is *normal* to this plane.

There are known cases of multiferroics with a relation between the spin structure and the polarization vector that is much more complex than suggested by the straightforward inverse Dzyaloshinskii–Moriya mechanism [12, 13]. A very representative example is the triangular lattice antiferromagnet  $\text{RbFe}(\text{MoO}_4)_2$  [29], where the electric polarization is exactly orthogonal to the helimagnetic planes. Cases like this require a more advanced symmetry-based treatment, as described in detail by Har-

ris [30]. In linarite, however, the proposed model of the I–III phase transition does not seem to involve a significant change in the magnetic-state symmetry. Hence, it is not clear why it would invoke a completely different type of coupling between magnetism and polarization. This is especially strange given that the observed direction of  $\mathbf{P}$  remains unchanged across the transition. Trying to make sense of this, we note that magnets with complex interactions often have very peculiar spin structures with multiple propagation vectors. One example is the spiral antiferromagnet  $\text{Ba}_2\text{CuGe}_2\text{O}_7$ , in which a very special antiferromagnetic cone phase described by simultaneous commensurate and incommensurate wave vectors was found [31]. The phenomenology of neutron diffraction observations in  $\text{Ba}_2\text{CuGe}_2\text{O}_7$  is remarkably similar to that in Phase III in linarite [16]. This analogy hints that Phase III in linarite may, in fact, also be a two- $Q$  structure, rather than a mixed phase like Phase II. This idea is consistent with the stable character of electric anomalies in Phase III, contrasting with the history-dependent behavior found in Phase II. Some more details regarding this possible structure are given in Appendix B. To summarize this discussion we just briefly note that in the case of  $\text{Ba}_2\text{CuGe}_2\text{O}_7$  the key to stabilizing this rather peculiar phase was the interplay of external field and anisotropic interactions (especially antisymmetric Dzyaloshinskii–Moriya interactions [32, 33]). In linarite the dramatic anisotropy of the phase diagram makes apparent the presence of non-negligible anisotropy in the interactions. At the same time, the antisymmetric geometry of the superexchange bond between the nearest  $\text{Cu}^{2+}$  neighbors allows the presence of Dzyaloshinskii–Moriya interactions, staggered along the chain.

#### D. Multiferroic metastability at low temperatures

As shown in Fig. 6, the situation with the isothermal magnetoelectric current becomes quite complicated as one reaches the region denoted II in the phase diagram (Fig. 2). The evidence from the previous studies is that this metastable region corresponds to the coexistence of domains of Phases I and IV. This picture agrees well with our present observations. In this regime a well-defined anomaly corresponding to a first-order transition is replaced by a family of extremely sharp peaks that show a strong history dependence. In fact, each such spike manifests the loss of stability of a single Phase I domain (with increasing field) or Phase IV domain (on decreasing field). The observed spikes are just a differential multiferroic analog of a familiar Barkhausen effect in ferromagnets.

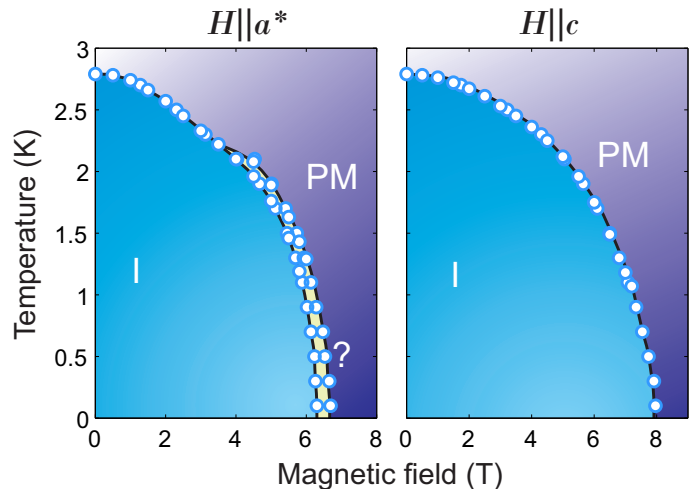


FIG. 15. Magnetic phase diagram of linarite deduced from electric current measurements for magnetic fields applied transverse to the  $\mathbf{b}$  direction. Left: Field along  $\mathbf{a}^*$ . The two dominant phases are Phase I and the disordered paramagnetic state. In high fields there is an additional intervening region, although it is not clear whether it represents a distinct thermodynamic phase. Right: Field along the  $\mathbf{c}$  direction. Symbols are experimental data; solid lines are guides for the eye.

#### E. Magnetic phase diagrams from electric measurements

The collected current data conveniently provide us with a way to reconstruct the magnetic phase diagram. The summary of our measurements is shown in Figs. 2 and 15. The phase diagram for the field applied in the  $\mathbf{b}$  direction is clearly the most interesting. Even though we find no electric activity in Phases IV and V, all the other ordered phases are proved to be multiferroic in nature.

We also find a peculiar behavior of the polarization vector (polarization reversal) near saturation for a magnetic field applied in the  $\mathbf{a}^*$  direction. According to Schäpers *et al.* [15], this phase diagram should contain a single elliptical spiral phase [34]. The abrupt reversal of polarization observed in our experiments is not necessarily indicative of a thermodynamic phase transition. It may just be the result of strong deformation of the spin structure by the magnetic field, as it becomes almost polarized. Nor can one fully exclude a spurious origin of this feature. The presence of misaligned grain in the sample may in principle result in this kind of behavior. On the other hand, the data for  $\mathbf{H} \parallel \mathbf{b}$  and  $\mathbf{H} \parallel \mathbf{c}$  taken from *the same sample* show no phase boundary “splitting” in applied magnetic fields. Whether or not there is an additional phase in this geometry near saturation remains an open question.

The phase diagrams for magnetic fields applied in the  $\mathbf{a}$ ,  $\mathbf{c}$  and  $\mathbf{c}^*$  directions undoubtedly contain just a single ordered phase with a conventionally looking phase boundary. In Fig. 15 we show just one such case with  $\mathbf{H} \parallel \mathbf{c}$ .



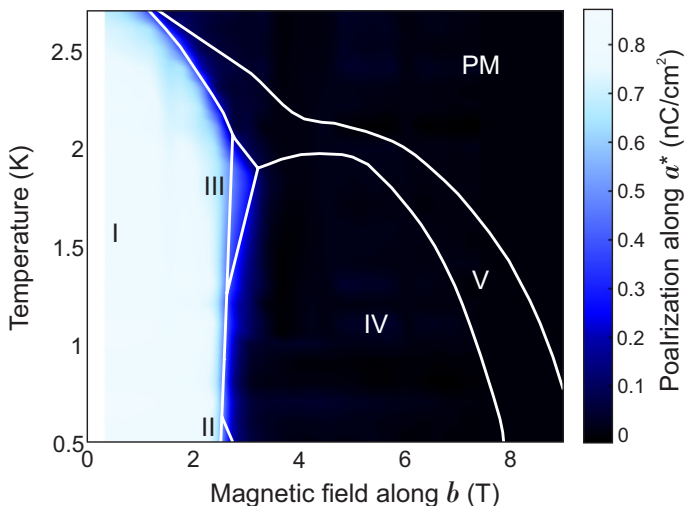


FIG. 16. False color map of  $P_{a^*}$  in a magnetic field along the  $b$  direction. Solid lines correspond to the phase boundaries according to [16].

## V. SUMMARY

At least three of linarite’s magnetic phases support spontaneous electric polarization: (i) The principal spin spiral state (Phase I) appears to be a classic “reverse Dzyaloshinskii–Moriya” improper ferroelectric. The observed direction of polarization is fully consistent with the magnetic structure proposed in Refs. [16, 18]. (ii) Also in agreement with Ref. [15], region II, found between the spiral Phase I and the collinear Phase IV, is actually a phase-separation regime, showing a typical history-dependent behavior of polarization. (iii) The polarization observed in Phase III is *not* consistent with the phase-separated magnetic state proposed in Ref. [16]. Rather, it appears to be a stable thermodynamic phase and may be a complex multi- $Q$  spin structure. (iv) A new region of polarization reversal, which may or may not be a distinct thermodynamic phase, is identified close to saturation for a magnetic field applied along the  $\mathbf{a}^*$  direction.

## ACKNOWLEDGMENTS

This work was supported by the Swiss National Science Foundation, Division 2. We also thank Dr. S. Gvasaliya (ETH Zürich) for support with experiments.

### Appendix A: The polarization map

The number of collected data allows us to reconstruct the  $P(H, T)$  surface. An example is shown in Fig. 16. Here the  $P_{a^*}$  component, reconstructed from the field scans is plotted. The region very close to  $H = 0$  is omitted here (due to nonlinearity of the sweep rate at the very

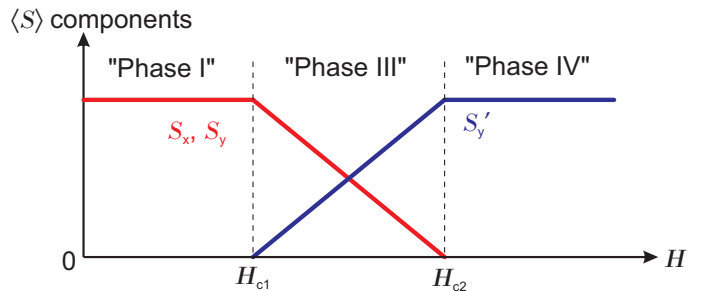


FIG. 17. Sketch of magnetic field dependence of the spin texture components  $S_x, S_y$  (of “Phase I”) and  $S'_y$  (of “Phase IV”) in the toy model. There is a region between  $H_{c1}$  and  $H_{c2}$  where both types of order coexist [as shown by Eq. (B1)]. This region corresponds to “Phase III”.

beginning of the scan). We also show the data at temperatures above Phase II only, as within this metastable phase no equilibrium polarization value can be consistently defined.

## Appendix B: The multi- $Q$ structure

### 1. A toy model

Before describing the plausible multi- $Q$  structure of Phase III in linarite, interpolating between Phases I and IV, we would like to consider a simplified toy model. This model serves as a nice illustration of the crossover between incommensurate and commensurate structures and is free of two major complications present in linarite: the ellipticity of the spiral phase and the noncoplanarity of the spin structures between Phases I and IV. In this two-dimensional toy model the low-field “Phase I” would be simply a circular spiral in the  $\mathbf{xy}$  plane ( $\mathbf{x}$  is the direction along the chain; the analog of  $\mathbf{b}$  in the real linarite structure, and  $\mathbf{y}$  is the analog of  $\mathbf{c}$ ). Then the “Phase I” order is described as  $\langle \mathbf{S}_{nm} \rangle = \mathbf{S}_y \cos(2\pi \mathbf{Q}_I \mathbf{r}_{nm}) + \mathbf{S}_x \sin(2\pi \mathbf{Q}_I \mathbf{r}_{nm})$ , with  $|\mathbf{S}_x| = |\mathbf{S}_y|$  and  $\mathbf{Q}_I = (\epsilon, 0.5)$  (here  $\epsilon$  is the incommensuration parameter; in Fig. 18  $\epsilon = 1/36$  is taken). The vector  $\mathbf{r}_{mn} = n\mathbf{x} + m\mathbf{y}$  simply enumerates the spin sites ( $n$  along the chain,  $m$  between the chains). In contrast, the commensurate order in “Phase IV” is simply  $\langle \mathbf{S}_{nm} \rangle = \mathbf{S}'_y \cos(2\pi \mathbf{Q}_{IV} \mathbf{r}_{nm})$ , where  $\mathbf{Q}_{IV} = (0, 0.5)$ .

Then the essential idea of constructing the spin texture of “Phase III” is to consider a linear combination of the two structures described above. The description of this complex ordering is given as:

$$\langle \mathbf{S}_{nm} \rangle = \mathbf{S}_y \cos(2\pi \mathbf{Q}_I \mathbf{r}_{nm}) + \mathbf{S}_x \sin(2\pi \mathbf{Q}_I \mathbf{r}_{nm}) + \mathbf{S}'_y \cos(2\pi \mathbf{Q}_{IV} \mathbf{r}_{nm}), \quad (\text{B1})$$

Within the toy model we may assume the dependence of  $\mathbf{S}_{\mathbf{x}, \mathbf{y}}$  and  $\mathbf{S}'_y$  on the external magnetic field as described in Fig. 17. Then in the region  $H_{c1} < H < H_{c2}$  we find a

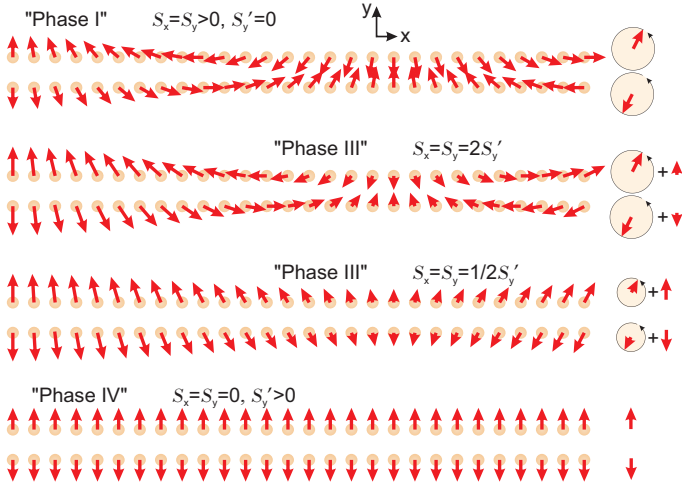


FIG. 18. Spin textures of the toy model, corresponding to different phases (and different magnetic-field strength). First comes the simple spiral “Phase I” at  $H < H_{c1}$ . Then there is “Phase III” [as given by Eq. (B1)], shown in two regimes: with a dominating spiral component ( $H \gtrsim H_{c1}$ ) and with a dominating antiferromagnetic component ( $H \lesssim H_{c2}$ ). The last phase is the straight antiferromagnetic “Phase IV” at  $H > H_{c2}$ .

complex type of order exhibiting propagation vectors  $\mathbf{Q}_I$  and  $\mathbf{Q}_{IV}$  simultaneously. The examples of the resulting spin structure in different regimes are given in Fig. 18.

## 2. Application to the actual Phase III of linarite

The structure of the actual Phase III of linarite is constructed from the known structures of Phases I and IV in direct analogy with the toy model, described above. The plausible spin arrangement is described as

$$\langle \mathbf{S}(\mathbf{r}) \rangle = \mathbf{S}_u \cos(2\pi \mathbf{Q}_I \mathbf{r}) + \mathbf{S}_b \sin(2\pi \mathbf{Q}_I \mathbf{r}) + \mathbf{S}_c \cos(2\pi \mathbf{Q}_{IV} \mathbf{r}). \quad (\text{B2})$$

Again,  $\mathbf{Q}_I = (0, 0.186, 0.5)$  and  $\mathbf{Q}_{IV} = (0, 0, 0.5)$  are the “original” propagation vectors of limiting single- $Q$  structures. Vector  $\mathbf{u}$  is the same as described in Sec. IV B. However, the complication [which makes the visualization of Eq. (B2) not very useful] is that the spin vector  $\mathbf{S}_c$  does not belong to the plane given by vectors  $\mathbf{S}_u - \mathbf{S}_b$  and is not orthogonal to this plane either. Ellipticity of the spiral contribution ( $\mathbf{S}_b > \mathbf{S}_u$ ) also adds to the overall complexity of the resulting structure. One has to keep in mind, that there is a significant ferromagnetic moment along the field direction  $\mathbf{b}$  present in Phase III as well (as the material is approximately one-third magnetized in this phase). This contribution is not included in Eq. (B2).

- 
- [1] D. I. Khomskii, “Multiferroics: Different ways to combine magnetism and ferroelectricity,” *J. Magn. Magn. Mater.* **306**, 1 (2006).
- [2] S.-W. Cheong and M. Mostovoy, “Multiferroics: a magnetic twist for ferroelectricity,” *Nat. Mater.* **6**, 13 (2007).
- [3] Y. Tokura, S. Seki, and N. Nagaosa, “Multiferroics of spin origin,” *Rep. Prog. Phys.* **77**, 076501 (2014).
- [4] T. Goto, T. Kimura, G. Lawes, A. P. Ramirez, and Y. Tokura, “Ferroelectricity and Giant Magnetocapacitance in Perovskite Rare-Earth Manganites,” *Phys. Rev. Lett.* **92**, 257201 (2004).
- [5] F. Kagawa, M. Mochizuki, Y. Onose, H. Murakawa, Y. Kaneko, N. Furukawa, and Y. Tokura, “Dynamics of Multiferroic Domain Wall in Spin-Cycloidal Ferroelectric  $\text{DyMnO}_3$ ,” *Phys. Rev. Lett.* **102**, 057604 (2009).
- [6] F. Schrettle, S. Krohns, P. Lunkenheimer, A. Loidl, E. Wulf, T. Yankova, and A. Zheludev, “Magnetic-field induced multiferroicity in a quantum critical frustrated spin liquid,” *Phys. Rev. B* **87**, 121105 (2013).
- [7] K. Yu Povarov, A. Reichert, E. Wulf, and A. Zheludev, “Giant dielectric nonlinearities at a magnetic Bose-Einstein condensation,” *Phys. Rev. B* **92**, 140410 (2015).
- [8] S. Park, Y. J. Choi, C. L. Zhang, and S.-W. Cheong, “Ferroelectricity in an  $s = 1/2$  chain cuprate,” *Phys. Rev. Lett.* **98**, 057601 (2007).
- [9] M. Mourigal, M. Enderle, R. K. Kremer, J. M. Law, and B. Fåk, “Ferroelectricity from spin supercurrents in  $\text{LiCuVO}_4$ ,” *Phys. Rev. B* **83**, 100409 (2011).
- [10] S. Seki, Y. Yamasaki, M. Soda, M. Matsuura, K. Hirota, and Y. Tokura, “Correlation between Spin Helicity and an Electric Polarization Vector in Quantum-Spin Chain Magnet  $\text{LiCu}_2\text{O}_2$ ,” *Phys. Rev. Lett.* **100**, 127201 (2008).
- [11] S. Furukawa, M. Sato, and S. Onoda, “Chiral Order and Electromagnetic Dynamics in One-Dimensional Multiferroic Cuprates,” *Phys. Rev. Lett.* **105**, 257205 (2010).
- [12] H. Katsura, N. Nagaosa, and A. V. Balatsky, “Spin current and magnetoelectric effect in noncollinear magnets,” *Phys. Rev. Lett.* **95**, 057205 (2005).
- [13] M. Mostovoy, “Ferroelectricity in spiral magnets,” *Phys. Rev. Lett.* **96**, 067601 (2006).
- [14] M. Baran, A. Jędrzejczak, H. Szymczak, V. Maltsev, G. Kamieniarz, G. Szukowski, C. Loison, A. Ormeci, S.-L. Drechsler, and H. Rosner, “Quasi-one-dimensional  $S = 1/2$  magnet  $\text{Pb}[\text{Cu}(\text{SO}_4(\text{OH})_2)]$ : frustration due to competing in-chain exchange,” *Phys. Status Solidi C* **3**, 220 (2006).
- [15] M. Schäpers, A. U. B. Wolter, S.-L. Drechsler, S. Nishimoto, K.-H. Müller, M. Abdel-Hafez, W. Schottenhamel, B. Büchner, J. Richter, B. Ouladdiaf, M. Uhlarz, R. Beyer, Y. Skourski, J. Wosnitza, K. C. Rule, H. Ryll, B. Klemke, K. Kiefer, M. Reehuis, B. Willenberg, and S. Süllow, “Thermodynamic properties of the anisotropic frustrated spin-chain compound linarite  $\text{PbCuSO}_4(\text{OH})_2$ ,” *Phys. Rev. B* **88**, 184410 (2013).
- [16] B. Willenberg, M. Schäpers, A. U. B. Wolter, S.-L.

- Drechsler, M. Reehuis, J.-U. Hoffmann, B. Büchner, A. J. Studer, K. C. Rule, B. Ouladdiaf, S. Süllow, and S. Nishimoto, “Complex Field-Induced States in Linarite  $\text{PbCuSO}_4(\text{OH})_2$  with a Variety of High-Order Exotic Spin-Density Wave States,” *Phys. Rev. Lett.* **116**, 047202 (2016).
- [17] Y. Yasui, M. Sato, and I. Terasaki, “Multiferroic Behavior in the Quasi-One-Dimensional Frustrated Spin-1/2 System  $\text{PbCuSO}_4(\text{OH})_2$  with  $\text{CuO}_2$  Ribbon Chains,” *J. Phys. Soc. Jap.* **80**, 033707 (2011).
- [18] B. Willenberg, M. Schäpers, K. C. Rule, S. Süllow, M. Reehuis, H. Ryll, B. Klemke, K. Kiefer, W. Schottenhamel, B. Büchner, B. Ouladdiaf, M. Uhlarz, R. Beyer, J. Wosnitza, and A. U. B. Wolter, “Magnetic Frustration in a Quantum Spin Chain: The Case of Linarite  $\text{PbCuSO}_4(\text{OH})_2$ ,” *Phys. Rev. Lett.* **108**, 117202 (2012).
- [19] A. U. B. Wolter, F. Lipps, M. Schäpers, S.-L. Drechsler, S. Nishimoto, R. Vogel, V. Kataev, B. Büchner, H. Rosner, M. Schmitt, M. Uhlarz, Y. Skourski, J. Wosnitza, S. Süllow, and K. C. Rule, “Magnetic properties and exchange integrals of the frustrated chain cuprate linarite  $\text{PbCuSO}_4(\text{OH})_2$ ,” *Phys. Rev. B* **85**, 014407 (2012).
- [20] H. G. Bachmann and J. Zemann, “Die Kristallstruktur von Linarit  $\text{PbCuSO}_4(\text{OH})_2$ ,” *Acta Crystallographica* **14**, 747 (1961).
- [21] Linarite crystals typically have a prismatic morphology with elongation along the  $b$  axis. In addition to this easily identifiable direction, typical prism also has the largest facet corresponding to  $[100]$  plane (the main cleavage plane of linarite). However, there is a reasonable chance of finding a crystal which has the  $[001]$  plane (the second cleavage plane) as the largest facet instead. These two cases were distinguished at the next step, where the x-ray diffraction check was performed.
- [22] As in the standard reciprocal lattice notation.
- [23] M. Schäpers, H. Rosner, S.-L. Drechsler, S. Süllow, R. Vogel, B. Büchner, and A. U. B. Wolter, “Magnetic and electronic structure of the frustrated spin-chain compound linarite  $\text{PbCuSO}_4(\text{OH})_2$ ,” *Phys. Rev. B* **90**, 224417 (2014).
- [24] I. E. Dzyaloshinskii, “Magnetoelectric Effect in Chromium Oxide,” *Sov. Phys. JETP* **10**, 628 (1960).
- [25] D. N. Astrov, “The Magnetoelectric Effect in Antiferromagnetics,” *Sov. Phys. JETP* **11**, 708 (1960).
- [26] D. N. Astrov, “Magnetoelectric Effect in Chromium Oxide,” *Sov. Phys. JETP* **13**, 729 (1961).
- [27] V. Dvořák, “Improper ferroelectrics,” *Ferroelectrics* **7**, 1 (1974).
- [28] M. Hälg, D. Hüvonen, T. Guidi, D. L. Quintero-Castro, M. Boehm, L. P. Regnault, M. Hagiwara, and A. Zheludev, “Finite-temperature scaling of spin correlations in an experimental realization of the one-dimensional Ising quantum critical point,” *Phys. Rev. B* **92**, 014412 (2015).
- [29] M. Kenzelmann, G. Lawes, A. B. Harris, G. Gasparovic, C. Broholm, A. P. Ramirez, G. A. Jorge, M. Jaime, S. Park, Q. Huang, A. Ya. Shapiro, and L. A. Demianets, “Direct transition from a disordered to a multiferroic phase on a triangular lattice,” *Phys. Rev. Lett.* **98**, 267205 (2007).
- [30] A. B. Harris, “Landau analysis of the symmetry of the magnetic structure and magnetoelectric interaction in multiferroics,” *Phys. Rev. B* **76**, 054447 (2007).
- [31] S. Mühlbauer, S. N. Gvasaliya, E. Pomjakushina, and A. Zheludev, “Double- $k$  phase of the Dzyaloshinskii-Moriya helimagnet  $\text{Ba}_2\text{CuGe}_2\text{O}_7$ ,” *Phys. Rev. B* **84**, 180406 (2011).
- [32] I. Dzyaloshinsky, “A thermodynamic theory of ‘weak’ ferromagnetism of antiferromagnetics,” *J. Phys. Chem. Solids* **4**, 241 (1958).
- [33] T. Moriya, “Anisotropic Superexchange Interaction and Weak Ferromagnetism,” *Phys. Rev.* **120**, 91 (1960).
- [34] Nonetheless, we note that the last non-featureless specific heat curve in the corresponding panel of Fig. 9 in Ref. [15] may give some room for speculation.